Spiky electric and magnetic field structures in flux rope experiments

W. Gekelman[a,1], S. W. Tang[a], T. DeHaas[a], S. Vincena[a], P. Pribyl[a], and R. Sydora[b]

[a]Department of Physics and Astronomy, University of California, Los Angeles, CA 90095; and [b]Department of Physics, University of Alberta, Edmonton, AB, Canada T6G 2R3

Edited by Snezhana I. Abarzhi, The University of Western Australia, Crawley, WA, Australia, and accepted by Editorial Board Member David A. Weitz May 27, 2018 (received for review December 8, 2017)

Magnetic flux ropes are structures that are common in the corona of the sun and presumably all stars. They can be thought of as the building blocks of solar structures. They have been observed in Earth's magnetotail and near Mars and Venus. When multiple flux ropes are present magnetic field line reconnection, which converts magnetic energy to other forms, can occur when they collide. The structure of multiple magnetic ropes, the interactions between multiple ropes, and their topological properties such as helicity and writhing have been studied theoretically and in laboratory experiments. Here, we report on spiky potential and magnetic fields associated with the ropes. We show that the potential structures are chaotic for a range of their temporal half-widths and the probability density function (PDF) of their widths resembles the statistical distribution of crumpled paper. The spatial structure of the magnetic spikes is revealed using a correlation counting method. Computer simulation suggests that the potential structures are the nonlinear end result of an instability involving relative drift between ions and electrons.

nonlinear structures | magnetic reconnection | flux ropes | colliding flux ropes | time domain structures

In many laboratory experiments and spacecraft observations, narrow spikes in electric potential were documented. For example, laboratory experiments on the propagation of high-power microwaves in density gradients have shown narrow regions of intense electric field where the incident electromagnetic wave frequency matched the local plasma frequency. These were called cavitons (1) as they were accompanied by depletions in density at these locations. These structures were subsequently seen in Earth's ionosphere using ground-based antennas in Arecibo, Puerto Rico (2, 3), as well as created in RF heating experiments based in Alaska (4). Other structures include electron phase space holes, which are Debye-scale size spikes that appear in the electric potential. They have been seen at a number of locations in space (5–7) and observed in the laboratory (8). It is possible that the electric fields associated with them scatter electrons and would lead to an enhanced electrical resistivity. Heat transport experiments (9) utilizing a small electron emitter in a background magnetoplasma reveal that the turbulence generated consists of Lorentzian-shaped electron temperature perturbations, which lead to an exponential power spectrum (10). Time domain structures (11) (TDSs), a name initially given to electric field packets detected by spacecraft (12), can be a moniker that includes all of the different aforementioned structures. Van Allen probe data indicate (13) the TDSs observed move along the magnetic field lines at speeds corresponding to that of 100- to 200-eV electrons. This was close to the electron thermal speed under their conditions and were identified as electron acoustic perturbations. TDSs, in general, occur over a large variety of scales ranging from as small as Debye lengths to the electron skin depth to possibly larger size across the magnetic field and up to Alfvénic wavelengths along the field. They are plentiful and are thought to be a nonlinear end state of turbulence. Here, we report the observation of both magnetic and potential structures embedded in magnetic flux ropes. They both exhibit narrow, spike-like temporal signatures but seem to be unrelated to one another. Using statistical techniques, we identify the spatial pattern associated with magnetic TDS (labeled by TDS_m) and also show the electric TDS_e is associated with magnetic reconnection in colliding ropes.

Magnetic flux ropes are structures with helical magnetic fields (and currents) and are known to occur throughout space and astrophysical plasmas (14, 15). What separates them from simple current filaments is that the azimuthal magnetic field associated with their current is large enough to cause them to become kink unstable, and interact with adjacent ropes if they are present. Flux ropes routinely occur within Earth's magnetopause boundary layer, and magnetotail. The surface of the sun is littered with flux ropes, which are visible as arched filaments when viewed in UV or X-ray emissions. Collisions of ropes that occur on the Sun can be mimicked in the laboratory if the flux ropes carry enough current to be kink unstable (16). When the kink current threshold is exceeded, each collision results in the conversion of some magnetic energy into heat, flows, and waves, which is fundamental to the processes of magnetic field line reconnection (17).

Experimental Setup

The flux rope experiments were performed in the large plasma device (LAPD) (18) at University of California, Los Angeles (UCLA). The plasma source is based on a 60-cm diameter barium oxide-coated cathode (19). A DC discharge is applied between the cathode and an anode placed 50 cm away, and is pulsed at a 1-Hz repetition rate for months at a time, using a high-power transistor switch

Significance

The phenomena investigated in this paper are relevant to the general subject of interfaces and mixing within the context of multiscale transport under nonequilibrium plasma conditions, and the phenomena fit well into the theme of this Special Feature. Magnetic flux ropes consist of helical magnetic fields with varying pitch, and on multiscale processes, such as induced magnetic and electric structures, become embedded in the magnetic flux ropes. Time domain structures (TDSs) spontaneously develop between the flux ropes and are associated with magnetic reconnection. The spiky nonlinear structures dominate the electric and magnetic field and are not described by a simple power law. They are not predicted by fluid theory and could be a major factor in the development of new turbulence theories.

Author contributions: W.G., S.W.T., T.D., S.V., P.P., and R.S. performed research; W.G., S.W.T., T.D., S.V., and R.S. analyzed data; W.G. wrote the paper; and S.V. and R.S. helped in writing/editing.

The authors declare no conflict of interest.

This article is a PNAS Direct Submission. S.I.A. is a guest editor invited by the Editorial Board.

Published under the PNAS license.

[1]To whom correspondence should be addressed. Email: gekelman@physics.ucla.edu.

This article contains supporting information online at www.pnas.org/lookup/suppl/doi:10.1073/pnas.1721343115/-/DCSupplemental.

Published online June 20, 2018.

Downloaded by guest on May 14, 2020

(20). The LAPD has over 450 access ports into which a variety of probes may be introduced using vacuum pump down stations. The plasma parameters are ($n_e < 3 \times 10^{12}$ cm^{-3}, $T_e = 4$–5 eV, $T_i =$ 1 eV, $\delta n/n = 3\%$, $L = 18$ m, diameter = 60 cm, He). A schematic of the experiment is shown in Fig. 1*B*. To create the flux ropes, a second cathode constructed from high-emissivity LaB_6 was inserted near the end of the device opposite to the plasma formation cathode. A second transistor switch connected to an anode located 11 m away powered the associated rope discharge. To create magnetic flux ropes, the LaB_6 cathode was masked forcing the electron emission through apertures cut in the mask, producing azimuthal magnetic fields large enough (5–30 G) to generate flux ropes.

Magnetic TDS_m

In the study of magnetic TDS_m, three experimental flux ropes geometries were used. In the first configuration (case 1), two ropes of diameter of 7.5 cm each were vertically separated by 1 cm (edge to edge) at their formation point. The total rope current was 600 A, with discharge voltage of $V_{rope} = 125$ V (5.8 A/cm^2, 850 W/cm^2). In the second configuration (case 2), two smaller ropes each with a diameter of 3 cm and horizontally separated by 1 cm ($I_D = 105$ A, $V_D = 210$ V, 7.8 A/cm^2, 500 W/cm^2) were generated. The third configuration (case 3) was that of a single flux rope with radius of 2.5 cm and with rope current and voltage of $I_{rope} = 130$ A and $V_{rope} = 100$ V (6.6 A/cm^2, 662 W/cm^2). Volumetric data at tens of thousands of locations and time steps ($\delta t = 3.2 \times 10^{-7}$ s, nt = 24,000) were acquired for all three configurations. The time derivative of the magnetic field was measured using three three-axis, 10 turn, differentially wound magnetic probes 3 mm in diameter. In the first two cases, a quasi-seperatrix layer (21), which is indicative of magnetic field line reconnection, was

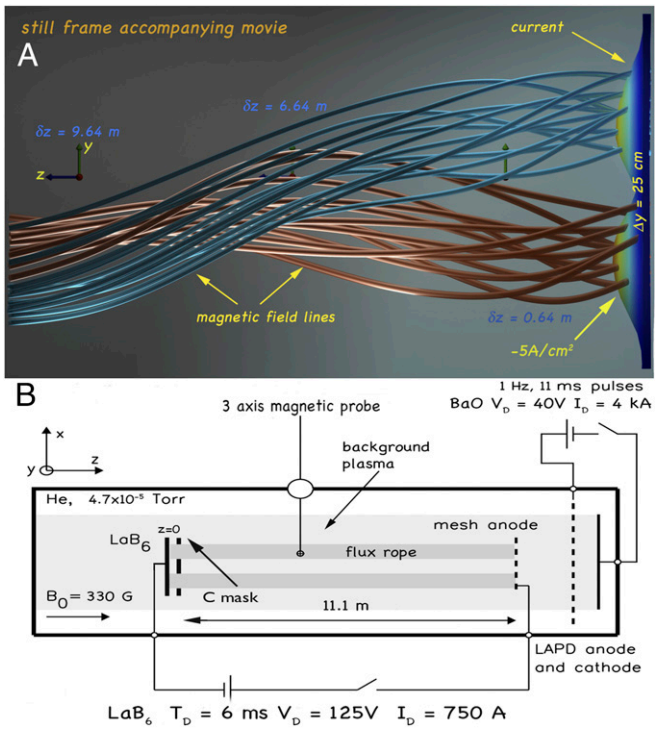

Fig. 1. (*A*) Magnetic field lines of two flux ropes (colored blue and orange) originating from the two unmasked regions of the 8-cm-diameter LaB_6 cathode. The surface and contours of the rope current density are shown on the right. The length along the *z* direction in this figure is 10 m. (*B*) Schematic of the experimental arrangement illustrating the background plasma production and the circuit used to switch on the ropes. The ropes start at $z = 0$. The motion of the ropes can be seen in Movie S1.

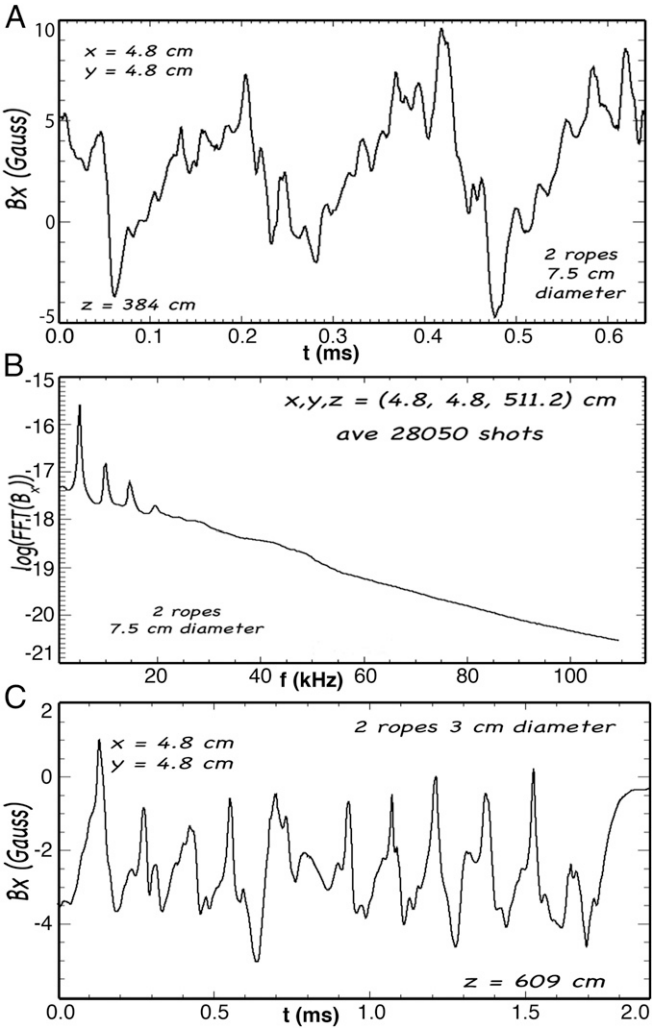

Fig. 2. (*A*) $B_x(t)$ for a single shot in case 1. The B-dot probe signal has been integrated and calibrated and is in gauss. (*B*) The average spectra of Bx on a log-linear scale showing an exponential tail at $f > 25$ kHz. The peaks at low frequency reflect the rotation of the ropes. (*C*) A single-shot trace of $B_x(t)$ for the smaller ropes in case 2, which have twice the discharge voltage compared with case 1 (*A*). The "spiky" nature of the magnetic field is clearly apparent.

observed. In case 1, magnetic field data were acquired at 2,810 spatial locations on each of 15 planes (64 cm $< z <$ 960 cm) transverse to the background magnetic field. A three-axis, magnetic reference probe was placed on the edge of the ropes. This was used to generate data necessary to average the data using a conditional trigger (22). The kink-unstable ropes were observed to twist about one another and move in an elliptical pattern with a frequency of about 5 kHz and periodically reconnect (17).

Fig. 2*A* shows a temporal trace of one component of the magnetic field, B_x, from one experimental instance of case 1. Fig. 2*B* shows the spectra of B_x measured by a separate probe fixed in position throughout the experiment in case 1. The fast Fourier transform (FFT) of each of the 28,050 shots was derived from the *x* component of the magnetic field averaged and then plotted on a log-linear scale as shown in Fig. 2*B*. The low-frequency oscillations appear as coherent peaks, and the exponential region is indicative of numerous Lorentzian pulses in the data (23). Using the following technique, an "average" spatial pattern of the magnetic field spikes was determined. First, a high-pass filter ($f > 25$ kHz) was applied to all three components of the magnetic field, to eliminate the kink signals. Next, an FFT was performed

Downloaded by guest on May 14, 2020

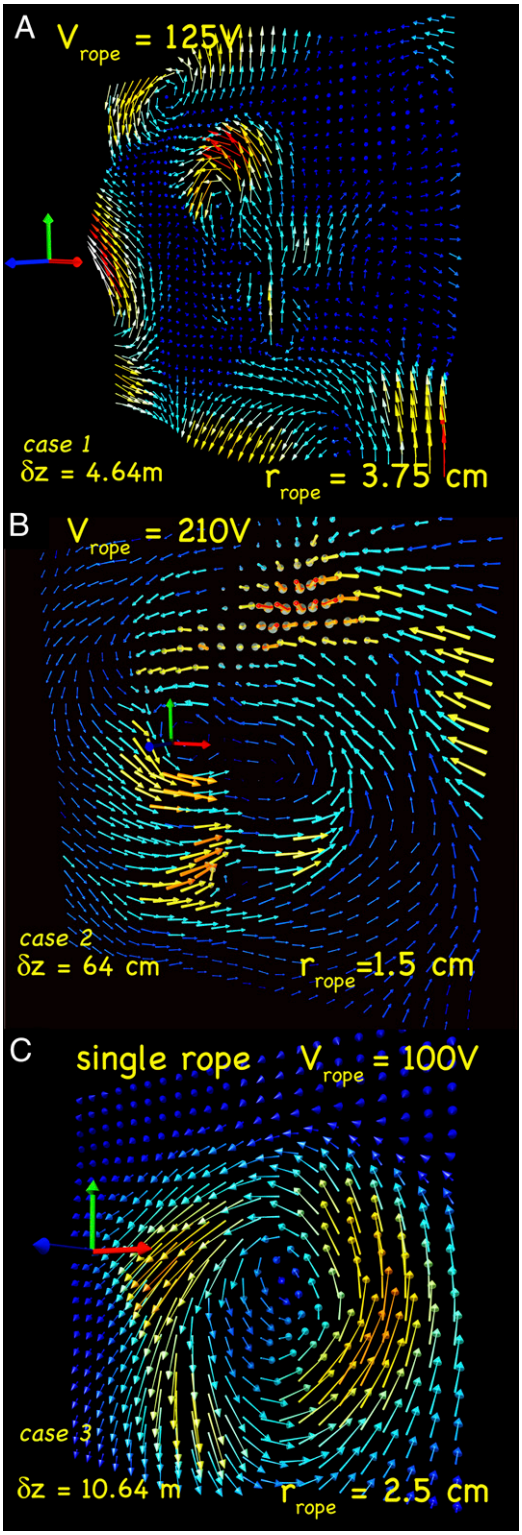

Fig. 3. Magnetic field of an average TDS_m for the three different cases showing their structure in plane transverse to the background magnetic field. (*A*) Case 1 flux ropes, 7.5-cm diameter each, are pictured in Fig. 1. V_{rope} is the rope discharge voltage, and the current density near the source of the ropes is 5 A/cm^2. (*B*) Case 2: smaller ropes with a higher discharge voltage. There are many more spikes in the magnetic signal, and the structure is more defined than in *A*. (*C*) Case 3 TDS_m morphology for a single flux rope. In all cases, δz is the distance of each rope to their point of origin.

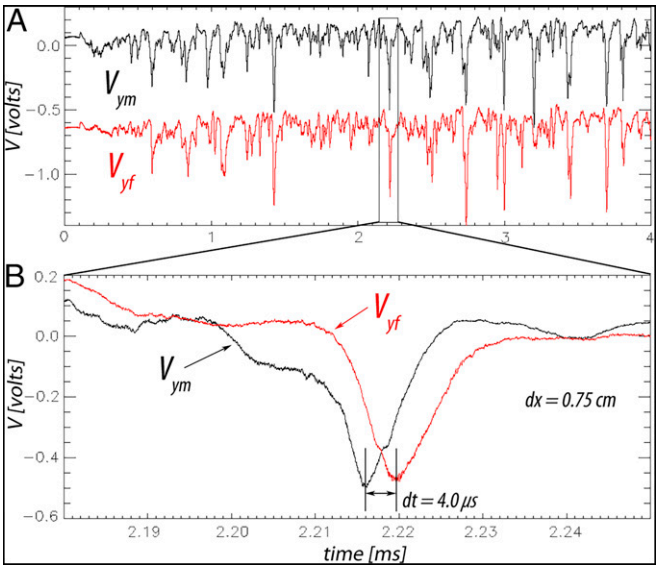

Fig. 4. (*A*) The first 4 ms of a typical shot of electric potential as a function of time from a single tip on the fixed probe (red trace) and a movable probe (black). (*B*) Expanded time series showing a 320-μs interval in *A*. A single TDS_e recorded by both probes. The approximate temporal width at half-maximum is estimated to be 100 μs. Each data sequence was acquired for 299,000 time steps (δt = 20 ns).

on each shot at every position. A Lorentzian pulse width, τ_L, is then determined by fitting a straight line to the exponential slope (Fig. 2*B*). In case 2 for the ropes shown in Fig. 3*B* (and a sample time trace in Fig. 2*C*), τ_L is 5 μs but differs from pulse to pulse. The pulse widths are normally distributed with a half-width at half-maximum of δt_L = 1 μs.

Using this method, a Lorentzian is constructed for the three components of **B**(t) each with the corresponding width, τ_L. The Lorentzians are then correlated with the filtered data and the points that exceed an 80% correlation coefficient threshold are stored. Their numbers and amplitudes are averaged at every probe location. If the spikes were completely random, then the magnetic field pattern would be vectors random in magnitude and orientation. This is not the case. The spike's magnetic field for the three cases is shown in Fig. 3.

We assume that the vector plots generated by the spike-counting method reflect the average instantaneous structure of an average TDS_m. In Fig. 3*A*, the spatial structure resembles that of the vertically displaced ropes observed in case 1 (Fig. 1*A*). The temporal magnetic field, shown in Fig. 2*A*, has sharp features and the 5-kHz rope oscillation is clearly visible. The case 2 flux ropes were also shown to be chaotic (24), and their corresponding pattern is shown in Fig. 3*B*. It reflects the side-by-side position of the ropes as seen in Fig. 1. In case 3, which is that of a single flux rope (25), there were no obvious sources of reconnection. However, TDS_ms were observed. The patterns seen in Fig. 3 are snapshots of the topology of an average TDS_m in three different cases. There is no a priori reason that the Lorentzian spikes have well-defined structure.

Magnetic spikes were also seen in a single flux rope experiment (26) at the University of Wisconsin–Madison and were attributed to internal reconnection, and a single rope was also observed after spheromak injection into a linear device (27). Fig. 3*C* is the TDS_m magnetic field pattern for the single flux rope case. The magnetic field of the TDS_m in all of these cases is on the order of 1 mG, which is much smaller (10^{-4} times) than that of the ropes themselves. The ropes can have azimuthal fields as large as 30 G. The transition from coherent to incoherent magnetic signals for a single rope (25) was shown to depend on the rope current, not the input power. In all three cases shown in

Downloaded by guest on May 14, 2020

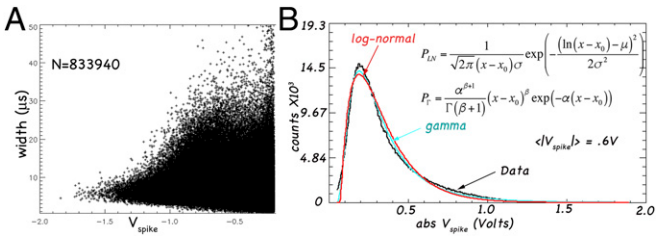

Fig. 5. (*A*) The distribution of spike width versus magnitude. *N* indicates the number of spikes used in the figure. Spikes with magnitude less than 0.1 V are not shown. (*B*) PDF of the spike amplitudes for one component of the fixed probe (Vx) shown in black. The blue curve is a log-normal distribution function fitted with least squares with $\sigma = 0.695$, $\mu = -0.879$, and $x_0 = 0.058$, while the red curve is a Gamma distribution with $x_0 = 0.1112$, $\beta = 1.410$, and $\alpha = 3.8256$. All parameters are fitted to within $\pm 10^{-4}$.

Fig. 3, the geometries differ considerably. However, the current density in cases 2 and 3 is larger than that of the first case. There are thousands more Lorentzian spikes shown in Fig. 3, and the patterns are better defined.

Electrostatic Pulses (TDS_e)

High-frequency potential and electric field data were acquired with three-axis electric dipole probes. Each of the six probe tips was the inner conductor of a high-frequency, Cu-clad, coaxial cable. Each tip measured the "floating" potential, and the voltage difference between each pair was used as a proxy for the electric field. The potential at each tip is obtained by terminating the signal with 50 Ω for the maximum temporal response, so it is not, strictly speaking, the floating potential. The probe current was on the order of 10 mA. Fig. 4 shows the potential as a function of time for one shot as measured on the tips of two probes. One probe is fixed at ($\delta x = \delta y = 0$, $\delta z = 767.8$ cm), while the other is movable and placed at the same (y, z) location and separated in x by 7.5 mm. The 4-μs delay between the signals indicates the TDS_es (Fig. 4*B*) move across the magnetic field at 1.9×10^5 cm/s. The spikes are not reproducible; they occur at different times and have a variety of heights for every occurrence of the flux ropes. They never exceed 2 V in magnitude and unlike the TDM_m are always negative. The potential spike half-width range from 1 to 50 μs, while electron phase space holes seen in the LAPD device (24) had lifetimes several times the inverse plasma frequency of 1–10 ns. The two probes were also used to correlate the signals. Thirty shots were stored at each location for both probes as the movable probe sampled 2,090 locations in the xz and xy planes. Single spikes were identified on both probes, and the distance between the probes and time delay from probe to probes indicated that the spikes moved in a plane transverse to the background field at approximately the ion sound speed. The data were used to calculate probability density functions (PDFs), spatial and temporal correlations, mean spatial locations, and average velocities of the spikes. The spike widths on three orthogonal tips as a function of amplitude are shown in Fig. 5*A*. Data in which the magnitude of the voltage was less than 0.1 V are not shown as they approach the noise. The largest spikes are seen to have the smallest widths.

The PDF of the spike magnitudes is shown in Fig. 5*B*, is well fitted with a log-normal distribution function, but is also very close to a shifted gamma distribution. These are coincidentally the same as the PDFs for the ridge lengths of a ball of crumpled paper (28, 29). The paper is crushed into a ball and sliced in half, and the length of each fold is determined and normalized to their average length. The PDF is a log-normal distribution function when the paper is crushed with a larger average radius of curvature per fold (weak containment) and a gamma distribution for tightly crushed folds. The analog for the electrostatic spikes could be how closely they are packed in space. Spikes that are near one another will repel one another, as they are all negative, analogous to the resistance of crushed paper to mechanical forces. In this experiment, the fit to the log-normal is slightly better, but the difference is, most likely, in the noise.

Where are the potential spikes located? The spatial distribution of the TDS_e spikes may be inferred from the average magnitude of all of the spikes counted at a particular x–y location. This is shown in Fig. 6 for a transverse (x–y) plane at $\delta z = 767.8$ cm. The largest spikes are seen in the reconnection region between the ropes, followed by smaller spikes in the gradient of the current at the edge of the ropes. To ascertain the spatial and temporal development TDS_e time sequences, as those shown in Fig. 4*A*, each time sequence was segmented into 21 bins and the TDS_e locations are plotted as Gaussian cones in Fig. 7. Three different times on the same plane are shown. The TDS_e structures populate the edge of the two ropes. The region between the ropes centered at (x, y) = (0, 1 cm) is where magnetic field line reconnection occurs. A quasi-seperatrix layer (30), a region in which magnetic field lines spatially diverge and indicative of reconnection, passes between the ropes. Fig. 7 indicates the position of the largest values of the TDS_es at three times on the same transverse plane. The data were synthesized by summing the results of 30 shots at each position together with the contributions from V_{+x}, V_{+y}, and V_{+z} on the moveable probe.

The data shown in Fig. 7 suggest that the TDS_es emanate from a reconnection region, which is described in detail in previous studies (22, 30). They subsequently migrate to the edge of the ropes, where as seen in Fig. 6 they are most likely to be found. One must not confuse the Gaussian spikes in Fig. 7, which serve as a visualization tool for location markers, with the actual shape of the TDS_es. Their structure can be deduced using 3D correlation analysis or spike counting as done with the magnetic signals. This will involve acquisition of a large amount of data (terabytes) and require weeks of machine time, and will be the subject of a future study.

What are these structures and do they affect the background plasma and feed back on the rope behavior? The flux ropes themselves were shown to be chaotic as evidenced from analysis of the Jensen–Shannon complexity and entropy (31–34). The chaos does not show up in averaged data as in Fig. 1*A*. Visualization of a chaotic structure would require 42,000 probes (or approximately the number of data points collected) recording all three components of the magnetic field in a single experimental instance.

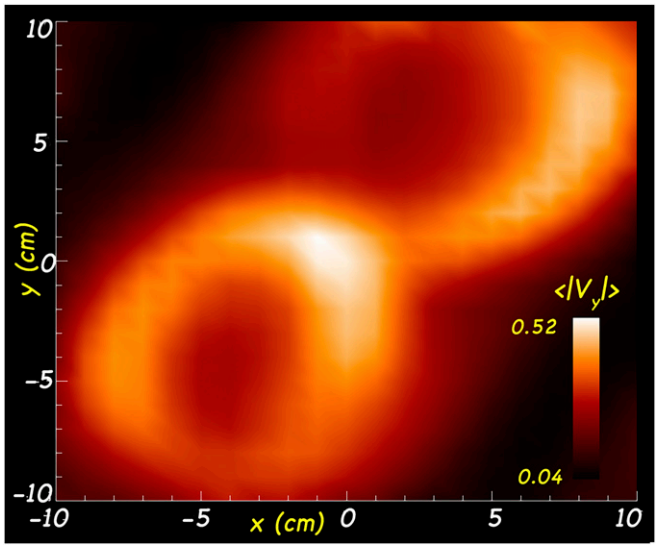

Fig. 6. The distribution of the magnitude of the potential spikes in a transverse plane at $z = 767.8$ cm. There are up to 1,890 spikes at each of the 441 locations on the plane at which data were acquired. The color bar shows the average of the absolute value of V_y in volts.

Downloaded by guest on May 14, 2020

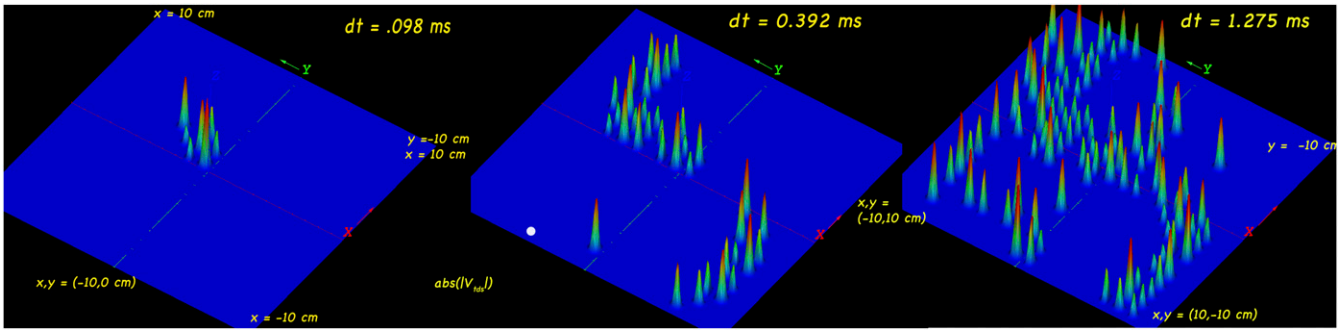

Fig. 7. The location of the TDS_e at three different times during the 6-ms interval shown in Fig. 4*A*. The TDS_es originate in the "X" point between the flux ropes, which is at the center of the plane, and evolve in time by moving along the periphery of the current channels. The height of the markers is proportional to the number of TDS_es at that location.

The first step in calculating the complexity is determination of the entropy. The Bandt–Pompe permutation entropy of a time series (31) allows for calculation of the entropy of a time series in the presence of noise. Just as in the entropy associated with thermodynamic systems, large entropy reflects disorder. The entropy is then used to determine the Jensen–Shannon complexity (32). These quantities are then used to construct a complexity entropy diagram on what is known as the C (complexity), H (normalized entropy) plane. The C–H plane is a plot of complexity on the ordinate and entropy on the abscissa. The C–H plane can distinguish deterministic chaos from random noise and has been used to study a variety of phenomena. For example, Zunino et al. (33) used the C–H plane to study an ammonia laser (chaotic), flow in a river (chaotic), the North American atmospheric oscillation (stochastic), crude oil and gold price dynamics (stochastic rather than deterministic), and human posture dynamics (noisy and chaotic). It was first used, for plasmas, to our knowledge by Maggs and Morales (34) to categorize electron temperature fluctuations in a transport experiment. It was then extended to the study of magnetic fluctuations in the flux rope experiment as described here (20). The methodology for constructing the C–H plane is described in detail in the previous two references (20, 34). These are shown with the data for the potential spikes (Fig. 8) as well as the complexity and entropy for several processes. For example, a sine wave appears on the lower left with small entropy and complexity. Highly random processes such as fractional Brownian motion have large entropy but small complexity, and are located are on the lower right. Also shown are several chaotic processes such as the Henon map, double pendulum, etc. These processes lead to chaotic time series but are described by iterative maps or differential equations. The points on the C–H plane are colored according to their frequency determined by their temporal half-width. The inverse of this frequency is interpreted as a representative spike width. Highly chaotic processes are in the center of the C–H plane having large complexity but midrange entropy. The very short-lived TDS spikes lie close to the fractional Brownian motion curve and are associated with random noise. The rest of the TDSs with lifetimes greater than 2 ms appear to be chaotic; the most chaotic TDSs have lifetimes on the order of 1–3 μs. The largest TDS_e voltages are on the order of −2.0 V. Two side-by-side probe tips spaced by 2 mm were used to get the temporal signature of the electric field, $\vec{E} = -\nabla V_p$, but could not be absolutely calibrated because of sheaths. The data suggest it could be as large as 100 V/m, but this is only an estimate.

Discussion and Conclusions

Magnetic and electrostatic TDSs have been observed in plasmas in association with flux ropes. The data indicate that they are not directly related. TDS_ms were observed in two different experiments involving flux rope collisions and have also been observed when there is only a single flux rope. Correlation of the magnetic signals (filtered well above the spike rotation frequencies) with Lorentzians generated using the exponential spectrum in the data, produced the morphology of the TDS_m. The structures resemble those of the ropes, but they are short-lived. The spatial patterns are a few meters in length and are lost when the flux ropes collide. In the single flux rope case, the patterns persist for 10 m. The potential structures are not Lorentzians and are chaotic for a range of their half-widths. Future correlation studies will determine their morphology. Previous work has shown that the magnetic fields associated with flux rope collisions are chaotic (24). A separate C–H plane analysis of the magnetic TDS_m shows they are chaotic as well.

The TDS_ms have very small magnetic fields and are not likely to scatter particles or affect the ropes. They may be thought as "magnetic foam," the detritus of the violent motion, heating, and electric fields of the ropes. The two-rope data suggest that reconnection can play a role in their formation.

The potential spikes, on the other hand, are quite large with potentials on the order of 10% of the background electron temperature. Electron bursts can contribute to the TDS_e, but it unlikely that they would slowly drift across the magnetic field as seen in Fig. 4*B*. Temperature fluctuations may contribute to the fluctuations (35), but experimental measurement of this is difficult. The electric potential TDS_es appear to originate in the reconnection region, and their magnitude is largest at the edge of the flux rope current channels. Rough estimates of their electric fields show they can scatter particles. A previous study has shown

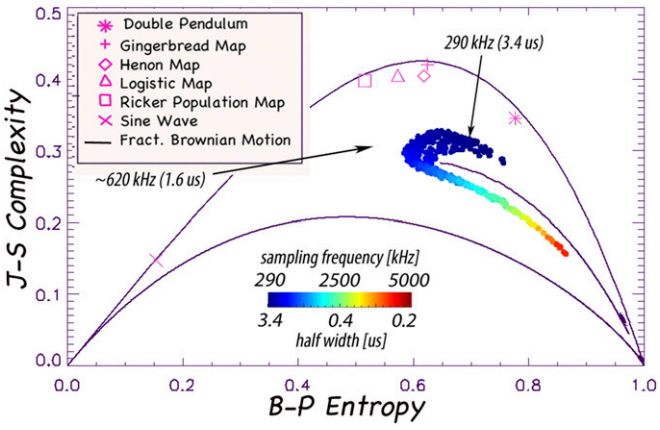

Fig. 8. C–H plane. The abscissa is the normalized Bandt–Pompe entropy, and the ordinate, the Jensen Shannon complexity. The data shown as colored dots are bordered by the minimum and maximum complexity curves. Points on the C–H plane are effectively colored by the half-width of the spikes found. Also shown are several iterative maps. Random noise that has large entropy and is not complex is seen on the lower right side on the fractional Brownian motion curve. The probe is located at (x, y, z) = (0, 0, 767.8 cm). Thirty 4.2-ms time series (δt = 0.66 μs) of Vx were used to generate this graph. The ion cyclotron frequency is 126 kHz.

Downloaded by guest on May 14, 2020

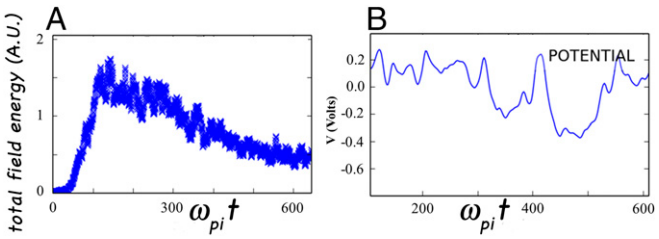

Fig. 9. Particle simulation of current-driven ion acoustic instability with initial relative electron–ion drift $V_{de} = 2C_s$, where C_s is the ion sound speed. Total electrostatic field energy (*A*) and electric potential (*B*) versus time at a fixed *x* position in the simulation.

that the ropes resistivity is anomalous and cannot be described by a local Ohm's law (36, 37). The TDS_es could play a role in this. From Fig. 3, we infer that the transverse scale size of the TDS_m is 3–10 cm, and from correlations the axial length is several meters. Preliminary correlation analysis indicates that the TDS_es have scale sizes on the order of 1 cm.

As a first step in understanding the origin of the electrostatic pulses, we consider a current-driven model where a relative electron–ion drift is assumed that exceeds the ion sound speed. In the experiment, the drift speed exceeds the sound speed by a factor of 4–5. A 2D particle-in-cell simulation model that follows electrons and ions and includes electron–ion collisions is used to model the growth and nonlinear evolution of the electric potential. A field-aligned current is initialized with drift speed that is twice the ion sound speed and as shown in Fig. 9*A* leads to the onset of current-driven ion acoustic instability that grows on the order of a few hundred inverse ion plasma periods. The ion acoustic instability is long known to be a candidate for anomalous resistivity in plasmas (38). Upon saturation of the instability nonlinear electric potential structures develop and drift slowly at approximately the ion sound speed. The dominant wavelength of the fluctuations at the onset of saturation is on the order of 0.1 λ_e, where λ_e is the electron–ion mean free path. For the experimental parameters, the mean free path is on the order of 15 cm; therefore, from the simulations, the dominant electrostatic potential fluctuation wavelength is roughly 1–1.5 cm and is orders of magnitude larger than the electron Debye length scale that would be dominant in a collisionless ion acoustic instability. This current-driven ion acoustic instability mechanism produces negative electrostatic potential dips, illustrated in Fig. 9*B*, that that have approximately the magnitude (approximately –0.2 to 0.4 V) and pulse width (~4–6 μs) of the TDSs that originate in the reconnection region of the experiment, which are then convected to the halo region of the flux ropes. Further investigation of this mechanism and the relation to magnetic spikes are being further explored and will be reported elsewhere.

ACKNOWLEDGMENTS. We thank George Morales for many useful discussions. We also thank Zoltan Lucky, Marvin Drandell, and Tai Ly for their expert technical support. Experiments were performed at the Basic Plasma Science Facility at UCLA and funded by the Department of Energy Office of Fusion Energy Research and the National Science Foundation (funded by Grants NSF-PHY-1036140 and DOE-DE-FC02-07ER54918).

1. Kim HC, Stenzel RL, Wong AY (1974) Development of cavitons and trapping of RF field. *Phys Rev Lett* 33:886–889.
2. Birkmayer W, Hagfors T, Kofman W (1986) Small-scale plasma-density depletions in Arecibo high-frequency modification experiments. *Phys Rev Lett* 57:1008–1011.
3. Duncan LM, Sheerin JP, Behnke RA (1988) Observations of ionospheric cavities generated by high-power radio waves. *Phys Rev Lett* 61:239–242.
4. Guzdar PN, et al. (2000) Diffraction model of ionosphereic irregularity-induced heater wave pattern detected on WIND satellite. *Geophys Res Lett* 27:317–320.
5. Coroniti F, Ashour-Abdalla M, Richard RL (1993) Electron velocity space hole modes. *J Geophys Res* 98:11349.
6. Ergun RE, et al. (1998) Debye scale plasma structures associated with magnetic field-aligned electric fields. *Phys Rev Lett* 81:826–829.
7. Franz JR, Kintner PM, Pickett JS, Chen L-J (2000) Properties of small amplitude electron phase-space holes observed by polar. *J Geophys Res Space Phys* 110:A09212.
8. Lefebvre B, et al. (2010) Laboratory measurements of electrostatic solitary structures generated by beam injection. *Phys Rev Lett* 105:115001.
9. Burke AT, Maggs JE, Morales GJ (1998) Observation of simultaneous axial and transverse classical heat transport in a magnetized plasma. *Phys Rev Lett* 81:3659–3662.
10. Pace DC, Shi M, Maggs JE, Morales GJ, Carter TA (2008) Exponential frequency spectrum and Lorentzian pulses in magnetized plasmas. *Phys Plasmas* 15:122304.
11. Mozer FS, et al. (2015) Time domain structures: What they are, what do they do and how they are made. *J Geophys Res* 42:3627–3638.
12. Wygant JR, et al. (2013) The electric fields and waves instruments on the radiation belt storm probes mission. *Space Sci Rev* 179:183–220.
13. Mozer FS, et al. (2013) Megavolt parallel potentials arising from double-layer streams in the Earth's outer radiation belt. *Phys Rev Lett* 111:235002.
14. Russell CT, et al. (1990) *Physics of Magnetic Flux Ropes*, AGU Geophysical Monograph Series (American Geophysical Union, Washington, DC), Vol 58.
15. Lukin S (2014) Self-organization in magnetic flux ropes. *Plasma Phys Contr Fusion* 56:060301.
16. Ryutov D, Furno I, Intrator T, Abatte S, Madziwa-Nussinov T (2006) Phenomenological theory off the kink instability in a slender plasma column. *Phys Plasmas* 13:032105.
17. Gekelman W, et al. (2016) Pulsating magnetic reconnection driven by three-dimensional flux-rope interactions. *Phys Rev Lett* 116:235101.
18. Gekelman W, et al. (2016) The upgraded large plasma device, a machine for studying frontier basic plasma physics. *Rev Sci Instrum* 87:025105.
19. Leneman D, Gekelman W, Maggs JE (2006) The plasma source of the large plasma device at UCLA. *Rev Sci Instrum* 77:015108.
20. Pribyl P, Gekelman W (2004) A 24 kA solid state switch for plasma discharge experiments. *Rev Sci Instrum* 75:669–673.
21. Priest ER, Démoulin P (1995) Three dimensional reconnection without null points I. Basic theory of magnetic flipping. *J Geophys Res* 100:23442.
22. Van Compernolle B, Gekelman W (2012) Morphology and dynamics of three interacting kink-unstable flux rope in a laboratory magnetoplasma. *Phys Plasmas* 19:102102.
23. Pace DC (2009) Spontaneous thermal waves and exponential spectra associated with a filamentary pressure structure in a magnetized plasma. PhD thesis (University of California, Los Angeles).
24. Gekelman W, Van Compernolle B, DeHaas T, Vincena S (2014) Chaos in magnetic flux ropes. *Plasma Phys Contr Fusion* 56:064002.
25. DeHaas T, Gekelman W, Van Compernolle B (2015) Experimental study of a linear/non-linear flux rope. *Phys Plasmas* 22:082118.
26. Brookhardt MI (2015) Subcritical onset of plasma fluctuations and magnetic self organization in a line-tied screw pinch. PhD thesis (University of Wisconsin–Madison, Madison, WI).
27. Gray T, Brown MR, Dandurand D (2013) Observation of a relaxed plasma state in a quasi-infinite cylinder. *Phys Rev Lett* 110:085002.
28. Sultan E, Boudaoud A (2006) Statistics of crumpled paper. *Phys Rev Lett* 96:136103.
29. Blair DL, Kudrolli A (2005) Geometry of crumpled paper. *Phys Rev Lett* 94:166107.
30. Lawrence EE, Gekelman W (2009) Identification of a quasiseparatrix layer in a reconnecting laboratory magnetoplasma. *Phys Rev Lett* 103:105002.
31. Bandt C, Pompe B (2002) Permutation entropy: A natural complexity measure for time series. *Phys Rev Lett* 88:174102.
32. Rosso OA, Larrondo HA, Martin MT, Plastino A, Fuentes MA (2007) Distinguishing noise from chaos. *Phys Rev Lett* 99:154102.
33. Zunino L, Soriano MC, Rosso OA (2012) Distinguishing chaotic and stochastic dynamics from time series by using a multiscale symbolic approach. *Phys Rev E Stat Nonlin Soft Matter Phys* 86:046210.
34. Maggs JE, Morales GJ (2013) Permutation entropy analysis of temperature fluctuations from a basic electron heat transport experiment. *Plasma Phys Contr Fusion* 55:085015.
35. Gennrich FP, Kendl A (2012) Analysis of the temperature influence on Langmuir probe measurements on the basis of gyrofluid simulations. *Plasma Phys Contr Fusion* 54:015012.
36. Gekelman W, et al. (2017) Non-local Ohms law during collisions of magnetic flux ropes. *Phys Plasmas* 24:070701.
37. Gekelman W, et al. (2018) Non-local Ohms law, plasma resistivity and reconnection during collisions of magnetic flux ropes. *Astrophys J* 853:33.
38. Papadopoulos K (1977) A review of anomalous resistivity for the ionosphere. *Rev Geophys Space Phys* 15:113.

Downloaded by guest on May 14, 2020